THE UNIVERSITY of EDINBURGH

Edinburgh Research Explorer

Theoretical model for the analysis of rotational behavior of penetrated mortise-tenon joints in traditional timber structures

Citation for published version:
Lu, W, Qiu, H & Lu, Y 2023, 'Theoretical model for the analysis of rotational behavior of penetrated mortise-tenon joints in traditional timber structures', *International Journal of Architectural Heritage: Conservation, Analysis and Restoration (International Journal of Architectural Heritage)*.
https://doi.org/10.1080/15583058.2023.2181720

Digital Object Identifier (DOI):
10.1080/15583058.2023.2181720

Link:
Link to publication record in Edinburgh Research Explorer

Document Version:
Publisher's PDF, also known as Version of record

Published In:
International Journal of Architectural Heritage: Conservation, Analysis and Restoration (International Journal of Architectural Heritage)

General rights
Copyright for the publications made accessible via the Edinburgh Research Explorer is retained by the author(s) and / or other copyright owners and it is a condition of accessing these publications that users recognise and abide by the legal requirements associated with these rights.

Take down policy
The University of Edinburgh has made every reasonable effort to ensure that Edinburgh Research Explorer content complies with UK legislation. If you believe that the public display of this file breaches copyright please contact openaccess@ed.ac.uk providing details, and we will remove access to the work immediately and investigate your claim.

Download date: 26. Mar. 2023

Theoretical model for the analysis of rotational behavior of penetrated mortise-tenon joints in traditional timber structures

Weijie Lu[a], Hongxing Qiu[a]* and Yong Lu[b]

[a]*School of Civil Engineering, Southeast University, Nanjing, China;*
[b]*Institute for Infrastructure and Environment, School of Engineering, The University of Edinburgh, Edinburgh, England*

Corresponding author:
Hongxing Qiu (Email: qhx101000854@163.com; Address: School of Civil Engineering, Southeast University, Nanjing 211189, China).

Theoretical model for the analysis of rotational behavior of penetrated mortise-tenon joints in traditional timber structures

Penetrated mortise-tenon joints (PMJs) are typical wood-to-wood connections commonly used in traditional Chinese timber structures. They play a crucial role in the structural behavior of timber constructions. This study derived a method of theoretical estimation for the rotational behavior of PMJs, which is unique and more comprehensive in that it takes both movement of the rotation center and bending deformation of the tenon into consideration. In addition, it experimentally and numerically validated the theoretical model, and quantitatively analyzed the position changes of the rotation center and the effect of the bending deformation. On this base, simplified calculation formulas are proposed for the prediction of equivalent elastic stiffness and peak moment of PMJs, and then applied for the calculation of the lateral stiffness of timber frames. As a result, the predicted lateral stiffness shows good agreement with test results, demonstrating the validity of the estimation method derived and its applicability to the structural analysis. The results of this study show that the rotation center of the tenon is not stationary, and its moving range in the horizontal direction is much larger than that in the vertical direction. Another pattern found is that the bending deformation of the smaller tenon counteracts more than 20% of the compressive deformation caused by the rigid-body motion, and therefore must be considered when analyzing the rotational behavior of PMJs.

Keywords: traditional timber structures; penetrated mortise-tenon joints; theoretical model; rotational behavior; moment-rotation relationship

1. Introduction

Timber structures have been widely used around the world for centuries. Mortise-tenon joints, a kind of wood-to-wood connections without any metal fasteners, are generally acknowledged as typical characteristics of traditional timber structures in China (Ma, 1991). It is known that historical timber architectures constitute a large portion of the cultural heritage in many countries. Unfortunately, many of these structures have seriously deteriorated due to aging, natural hazards and man-made accidents (Poletti et

al., 2019; Xie et al., 2018), causing an urgent demand for the preservation of these architectural heritages. Besides vintage buildings, new-built traditional timber structures have also gained increasing popularity in the field of public buildings due to the rapid development of tourism and the growing emphasis on green buildings in China. However, there is a lack of specific analytical methods for traditional timber structures incorporating mortise-tenon joints in existing codes, e.g. the latest Chinese specification GB50005-2017 (2017), with the fact that the structural design of such constructions remains enabled mainly by tradition and empirical knowledge. It has been repeatedly shown in previous studies that the structural performance of traditional timber structures is significantly influenced by the rotational behavior of the mortise-tenon joints (Eckelman and Haviarova, 2008; King et al., 1996; Seo et al., 1999). For the sake of reasonable design for traditional timber structures, there remains a strong need for further investigation into the appropriate analysis and estimation of the rotational behavior of mortise-tenon joints.

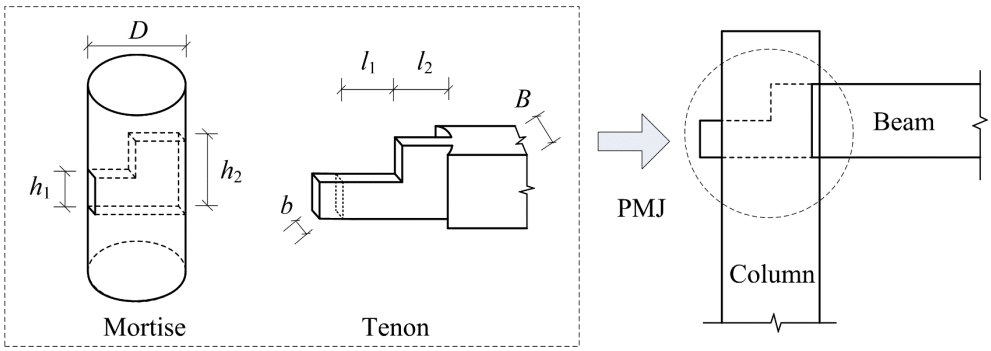

Figure 1. Configuration and geometric parameters of PMJ

Penetrated mortise-tenon joints (PMJs) represent a commonly encountered type of mortise-tenon joints in traditional timber structures, whose configuration is shown in Figure 1. The joint is formed by inserting a tenon at the tip of the beam into a mortise at the column. As the name implies, the tenon of the PMJ usually penetrates through columns with different cross-sections at the root and the front segments, which are called the larger tenon and smaller tenon respectively. For the sake of aesthetic requirements

and reducing drilling damage to columns, the height of the smaller tenon is usually half of the larger tenon (Ma, 1991). This special configuration with different cross-sections makes it more complicated to analyze the force mechanism of PMJs compared to other mortise-tenon joints with relatively simple geometric features.

Many experimental studies on PMJs have provided valuable insight into the rotational behavior of this connection. Preliminary tests found that PMJs exhibit semi-rigid characteristics and have better seismic performance than other types of traditional joints (Zhao et al., 2010). Chen and Qiu (2016) and Chun et al. (2016) indicated that the geometric features, summarized in Figure 1 left, govern the complex load-carrying mechanism of PMJs. Gao et al. (2015) suggested that PMJs with larger friction coefficients have better capacities of energy dissipation. The influence of gaps on the mechanical performance of PMJs was investigated by Xue et al. (2020) and He (2019). They clarified that looseness leads to the initial slip of the joints and reduces the rotational stiffness and bearing capacity.

It is worth noting that most of the previous studies on PMJs have focused on experimental investigations, and there is a lack of an appropriate analytical model for the calculation of the stiffness and strength of this kind of joint. Some researchers have started paying more attention to this aspect. Chun et al. (2016) proposed a trilinear model to represent the behavior of PMJs by fitting experimental data. Although the simplified model shows good agreement with test results, it does not apply to other joints whose geometric and material parameters differ from the specimens. Ma et al. (2020) derived a simplified equation for predicting the moment-rotation relationship of PMJs after investigating the embedded compressive mechanism. Similarly, a theoretical model of PMJs considering different working states was proposed by He et al. (2021). Despite preliminary validation by their individual experiments, the general applicability of these

models is not clear due to restrictions in the assumptions being made. For instance, the rotation center of the tenon was assumed as different fixed positions (He et al., 2021; Ma et al., 2020; Ogawa et al., 2016), which are inconsistent with each other and also contradict the argument that the rotation center may move according to the balances of the load and reactions (Tanahashi and Suzuki, 2012). Furthermore, the bending deformation of the tenon was ignored in the aforementioned models while Zhang et al. (2018) suggested that neglecting the bending deformation could cause considerable errors.

The aim of the work presented herein was to develop an improved theoretical model with general applicability for the analysis of the rotational behavior of PMJs, specifically the moment-rotation relationship. A particular focus is placed on taking both the movement of the rotation center and the bending deformation of the tenon into consideration. The importance of addressing these two factors when dealing with PMJs was carefully investigated in the subsequent discussion. Then, simplified calculation methods were proposed for the prediction of equivalent elastic stiffness and peak moment of PMJs, which were validated against a wide range of available experimental data on PMJ specimens. Finally, the simplified theoretical model was applied for the calculation of the lateral stiffness of a wooden portal frame with PMJs, exploring the applicability and accuracy for the analysis of traditional timber structures.

2. Theoretical model

2.1 Basic mechanism

Due to wood shrinkage, loading history or poor maintenance, PMJs often involve gaps between the mortise and the tenon. When subjected to lateral loads, the tenon of loose PMJs will rotate initially around the edge of the mortise without engaging any moment

resistance, i.e. as rigid-body motion. The moment resistance of the joint starts increasing when the tenon contacts the mortise. The compressive forces appear in the local regions where the compressive deformation happens. Frictional forces are also produced if the contact surfaces tend to slide. The compressive and frictional forces acting on local compression regions of the tenon are illustrated in Figure 2(a)(b). In passing, a specific illustration of subscripts for local compression regions is included in Table S1 of the supplemental material. These forces in combination produce a resisting moment that

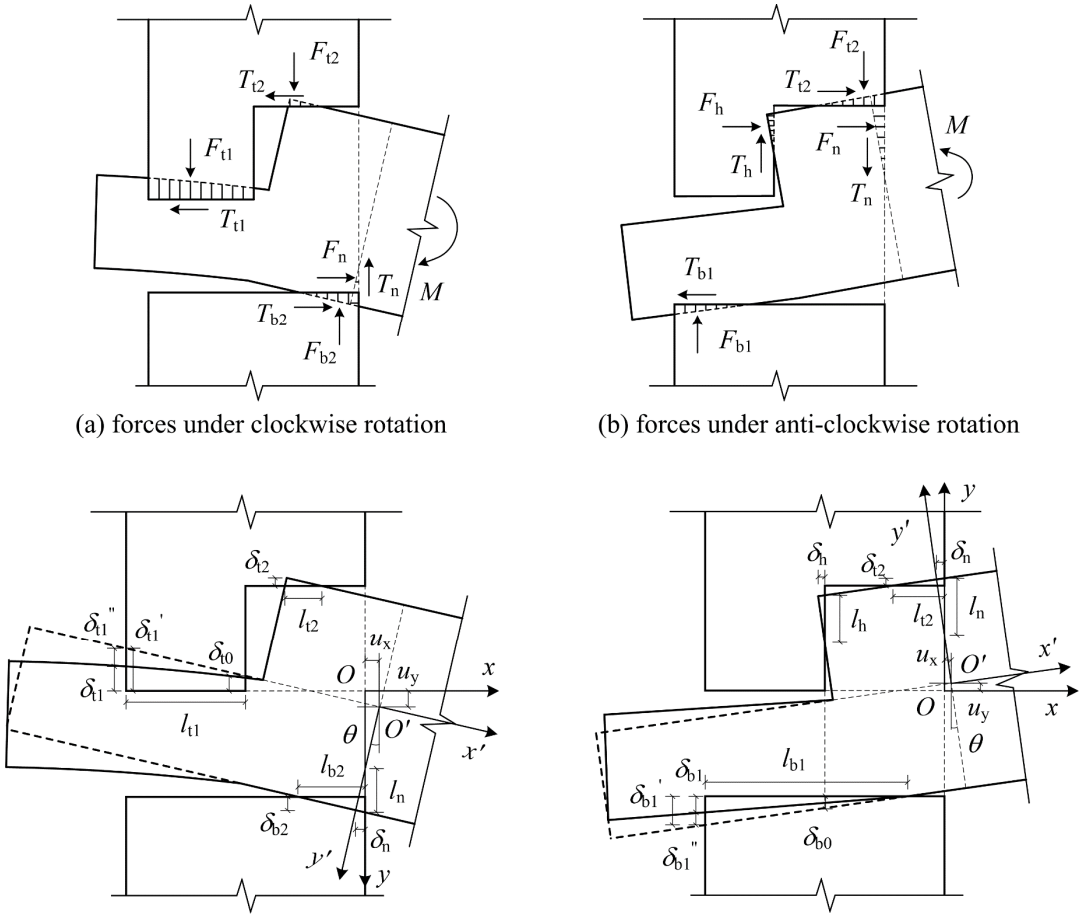

(a) forces under clockwise rotation (b) forces under anti-clockwise rotation

(c) deformation under clockwise rotation (d) deformation under anti-clockwise rotation

counter-balances the moment induced by external forces.

Figure 2. Force analysis and compressive deformation of the tenon

It can be understood that a larger rotation angle produces larger plastic compressive deformation, which means stronger interaction between the mortise and the tenon, thus resulting in a larger moment resistance of the joint. The increasing rate of the

moment resistance will only slow down when the wood in the compression regions begins to yield.

Due to the asymmetric shape of the tenon section, PMJs have been demonstrated to exhibit distinct failure features under clockwise and anti-clockwise rotation (Chen and Qiu, 2016). Under clockwise rotation, the tenon will be torn along the grain in the variable cross-section when the stress exceeds the tensile strength. While rotating in the anti-clockwise direction, the bending failure will tend to appear in the lower part of the tenon when the stress exceeds tensile strength along the grain.

2.2 Assumptions

To derive the theoretical model, several basic assumptions are adopted in this study, some of which are generally recognized in the related literature.

1. The properties of wood are described only in two directions, namely along and across the grain (Nowak et al., 2013).

2. Due to the different heights of cross-sections, the bending deformation is considered negligible for the larger tenon (Pan et al., 2015) but noticeable for the smaller tenon (Zhang et al., 2018).

3. The compressive deformation between the mortise and tenon is considered to take place across the grain because the modulus of elasticity (MOE) parallel to the grain is significantly larger than that perpendicular to the grain (Chang et al., 2006; Ma et al., 2020).

4. The constitutive law of compression across the wood grain is simplified as an ideal elastic-plastic model (He et al., 2021):

$$\sigma = \begin{cases} E_{\mathrm{c,R}}\varepsilon & ,0 \le \varepsilon \le \varepsilon_{\mathrm{cy,R}} \\ f_{\mathrm{c,R}} & ,\varepsilon_{\mathrm{cy,R}} \le \varepsilon \le \varepsilon_{\mathrm{cu,R}} \end{cases} \tag{1}$$

where $f_{c,R}$ and $E_{c,R}$ are the compressive strength and the MOE across the grain, $\varepsilon_{cy,R}$ and $\varepsilon_{cu,R}$ are the yield and ultimate compressive strain, respectively.

5. In the elastic stage of the wood, the compressive stress is proportional to the deformation (Pan et al., 2015):

$$\sigma_i = \delta_i E_{c,R} / k_i h_i \tag{2}$$

where δ_i is the compressive deformation; h_i represents the physical heights of compression regions; k_i is the equivalent height coefficient that is determined by the distribution of compression strain along the forced direction (Chen et al., 2016).

6. The friction coefficient of the wood contact surfaces is assumed to be constant during the rotation process of the tenon. The frictional forces can be calculated according to Coulomb's law of friction (Chang and Hsu, 2007; Ma et al., 2020).

2.3 Derivation of key equations

The process of establishing the theoretical model is mainly divided into seven steps based on the above assumptions. The flowchart of analysis procedures is shown in Figure S1.

For PMJs with gaps, the gap-induced initial rotation θ_0 can be expressed as:

$$\begin{cases} \theta_0^+ = \min\left\{ \arcsin\left(\dfrac{h_2 + h_{02}}{\sqrt{h_2^{\,2} + l_2^{\,2}}}\right) - \arcsin\left(\dfrac{h_2}{\sqrt{h_2^{\,2} + l_2^{\,2}}}\right), \arctan\left(\dfrac{h_{01}}{D}\right) \right\} \\ \theta_0^- = \min\left\{ \arctan(h_{01}/l_1), \arctan(h_{02}/D) \right\} \end{cases} \tag{3}$$

where the superscripts "+" and "–" indicate the clockwise and anti-clockwise rotation, respectively; h_{01} and h_{02} are the initial gaps on the smaller and larger tenon, respectively.

Only when the rotation angle exceeds θ_0 can the joint start resisting the external loads. The following sections will focus on the theoretical deduction of the moment-

rotation relationship of the PMJs based on geometric, physical and equilibrium conditions.

2.3.1 Geometric conditions

The intersection of the horizontal axis and column edge is defined as reference point O, and the intersection of the beam axis and tenon neck is defined as displaced point O'. The horizontal displacement, vertical displacement, and rotation angle between the displaced point O' and reference point O are represented by u_x, u_y, and θ respectively, as shown in Figure 2(c)(d). By taking the reference point O and the displaced point O' as the origins, the global coordinate system oxy and the local coordinate system $o'x'y'$ are established respectively. The former is stationary while the latter follows the rigid-body motion of the tenon. The relationship between these two systems can be expressed as:

$$\begin{bmatrix} x' \\ y' \end{bmatrix} = \begin{bmatrix} \cos\theta & -\sin\theta \\ \sin\theta & \cos\theta \end{bmatrix} \begin{bmatrix} x \\ y \end{bmatrix} + \begin{bmatrix} u_x \\ u_y \end{bmatrix}$$

Then, the coordinate transformation of every point in the tenon during the rotation of the joint can be calculated. Based on the geometric relationship shown in Figure 2(c)(d), the compressive deformation δ_i caused by the rigid-body motion and the corresponding compression length l_i can be expressed as follows.

For clockwise rotation:

$$\begin{cases} \delta_{t1}^{'} = \tan\theta(D + u_x) - u_y - h_{01} \\ \delta_{t0} = \tan\theta(l_2 + u_x) - u_y - h_{01} \\ \delta_{t2} = l_2 \sin\theta - (h_2 - h_1)(1 - \cos\theta) - u_y - h_{02} \\ \delta_{b2} = h_1(\sec\theta - 1) - u_x \tan\theta + u_y \\ \delta_n = h_1 \sin\theta - u_x \end{cases} \tag{4}$$

$$l_i = \begin{cases} \delta_i / \sin\theta\cos\theta, & i = t_2, n \\ \delta_i / \tan\theta, & i = t_1, b_2 \end{cases} \tag{5}$$

where l_{t1} will be replaced by l_1 if the value of $\delta_{t1}'/\tan\theta$ exceeds l_1.

For anti-clockwise rotation:

$$\begin{cases} \delta_{b1}' = \tan\theta(D+u_x)+h_1\left(\sec\theta-1\right)-u_y-h_0 \\ \delta_{b0} = \tan\theta(l_2+u_x)+h_1\left(\sec\theta-1\right)-u_y-h_0 \\ \delta_{t2} = (h_2-h_1)\left(\sec\theta-1\right)-u_x\tan\theta+u_y-h_{02} \\ \delta_{h} = (h_2-h_1)\sin\theta-l_2\left(1-\cos\theta\right)-u_x \\ \delta_{n} = (h_2-h_1)\sin\theta-u_x \end{cases} \tag{6}$$

$$l_i = \begin{cases} \delta_i/\sin\theta\cos\theta, & i=\mathrm{h,n} \\ \delta_i/\tan\theta \quad\quad , & i=\mathrm{t_2,b_1} \end{cases} \tag{7}$$

where h_0=min{h_{01}, h_{02}} and l_{b1} will be replaced by D if the value of $\delta_{b1}'/\tan\theta$ exceeds D.

Specially, the compressive deformation of the smaller tenon needs to be modified to consider the influence of the bending deformation. In essence, the compressive deformation of the smaller tenon δ_{i1} is the superposition of the rigid-body displacement δ_{i1}' and the bending deformation δ_{i1}''. Their relationship is further illustrated by Equation (8), and can also be seen in Figure 2(c)(d). The compressive deformation caused by rigid-body displacement is distributed linearly along the length direction of the smaller tenon while that caused by bending deformation is distributed nonlinearly. After superposition, the final deformation is still nonlinearly distributed. To simplify the calculation, the actual compressive deformation is modified as linear distribution along the length direction based on the principle of equivalent deflection at the top of the smaller tenon.

$$\delta_{i1} = \delta_{i1}' - \delta_{i1}'' \tag{8}$$

To calculate the bending deformation, the smaller tenon is simplified as a cantilever beam. The simplified calculation is schematically shown in Figure S2 of the supplemental material. The relationship between the linear load of the cantilever beam q_i

and the compressive stress of the smaller tenon σ_i can be expressed as $q_i=b\sigma_i$. The bending deformation of the smaller tenon can then be obtained by Equation (9) based on the method of graph multiplication.

$$\delta_{i1}^{''}=\frac{(4q_{i0}+11q_{i1})l_1^4}{120EI}=\frac{(4\sigma_{i0}+11\sigma_{i1})l_1^4}{10Eh_1^3} \tag{9}$$

where E is the bending modulus of elasticity; I is the inertia moment of the smaller tenon.

Based on Equations (2)(4)(6)(8)(9), the actual compressive deformation of the smaller tenon can be expressed by the principle of deformation compatibility.

$$\begin{cases}\delta_{\mathrm{t1}}=\dfrac{\tan\theta(D+u_{\mathrm{x}})-u_{\mathrm{y}}-h_{01}}{1+\lambda\dfrac{E_{\mathrm{c,R}}l_1^4}{k_{\mathrm{t}}Eh_1^4}}\\ \delta_{\mathrm{b1}}=\dfrac{\tan\theta(D+u_x)+h_1\left(\sec\theta-1\right)-u_y-h_0}{1+\lambda\dfrac{E_{\mathrm{c,R}}l_1^4}{k_{\mathrm{b}}Eh_1^4}}\end{cases} \tag{10}$$

where λ is determined by Equation (9) and depends on the stress distribution of the smaller tenon. If the root segment of the smaller tenon has not contacted the mortise ($\sigma_{i0}=0$), λ is 1.1; Otherwise, λ is 1.5.

2.3.2 Physical conditions

The compressive stress is expressed by Equation (2) when the wood remains elastic. After yielding, the stress equals the compression strength across the grain according to Equation (1). To calculate the compressive forces and lever arms in the elastoplastic state, β_i and α_i are defined by Equations (11) and (12) respectively. The force modification factor β_i represents the ratio of the actual plastic force F_2 to the hypothetical elastic force F_1 while

the lever arm modification factor α_i considers the position change of the resultant point of compressive forces after wood yielding, as illustrated in Figure 3.

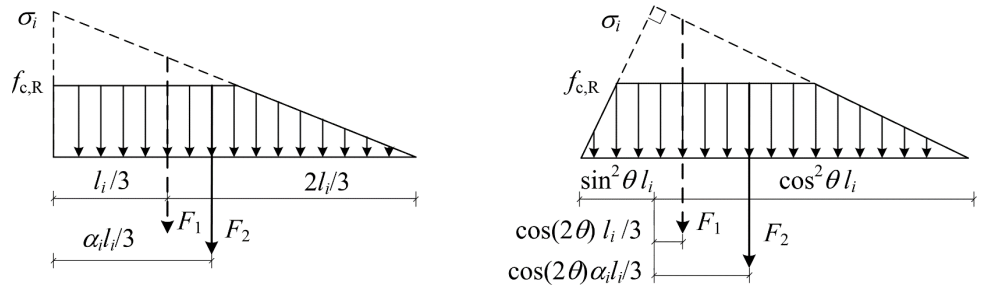

(a) region-b_1, b_2, t_1, t_2^- (b) region-h, n, t_2^+

Figure 3. Compressive stress of local regions in the elastoplastic stage

$$\beta_i = \begin{cases} 1 & ,0 \le \delta_i < \delta_{y,i} \\ 1-(1-\delta_{y,i}/\delta_i)^2 & , \quad \delta_i \ge \delta_{y,i} \end{cases} \tag{11}$$

$$\alpha_i = \begin{cases} 1 & ,0 \le \delta_i < \delta_{y,i} \\ \dfrac{1-(1-\delta_{y,i}/\delta_i)^3}{1-(1-\delta_{y,i}/\delta_i)^2} & , \quad \delta_i \ge \delta_{y,i} \end{cases} \tag{12}$$

where $\delta_{y,i}$ represents the compressive deformation when wood yielding, which can be calculated according to Equation (2) by replacing σ_i with $f_{c,R}$.

Based on Equations (2)(5)(7)(11), the compressive forces can be obtained as:

$$F_i = 0.5\beta_i b_i l_i \sigma_i \tag{13}$$

where b_i is the width of the local compression regions: $b_{t1}=b_{t2}=b_{b1}=b_{b2}=b_h=b$, $b_n=B-b$. In particular, the compressive force of the top surface of the smaller tenon F_{t1} should be revised to $0.5bl_1(\sigma_{t1}+\sigma_{t0})$ when the root segment of the smaller tenon contacts the mortise under clockwise rotation.

Based on Coulomb's law, frictional forces can then be obtained as

$$T_i = \mu F_i \tag{14}$$

The arms of compressive forces under clockwise and anti-clockwise rotation can be calculated by Equations (15) and (16) respectively. The reference point *O* is considered as the point for calculating moments.

$$\begin{cases} X_{\mathrm{t1}} = D - l_{\mathrm{t1}}\,\alpha_{\mathrm{t1}}/3 \\ X_{\mathrm{t2}} = l_2\cos\theta - (h_2 - h_1)\sin\theta - u_{\mathrm{x}} - l_{\mathrm{t2}}\cos(2\theta)\,\alpha_{\mathrm{t2}}/3 \\ X_{\mathrm{b2}} = l_{\mathrm{b2}}\alpha_{\mathrm{b2}}/3 \\ X_{\mathrm{n}} = h_1\cos\theta + u_{\mathrm{y}} - l_{\mathrm{n}}\cos(2\theta)\,\alpha_{\mathrm{n}}/3 \end{cases} \tag{15}$$

$$\begin{cases} X_{\mathrm{t2}} = l_{\mathrm{t2}}\,\alpha_{\mathrm{t2}}/3 \\ X_{\mathrm{b1}} = D - l_{\mathrm{b1}}\alpha_{\mathrm{b1}}/3 \\ X_{\mathrm{h}} = (h_2 - h_1)\cos\theta - l_2\sin\theta + u_{\mathrm{y}} - l_{\mathrm{h}}\cos(2\theta)\,\alpha_{\mathrm{h}}/3 \\ X_{\mathrm{n}} = (h_2 - h_1)\cos\theta + u_{\mathrm{y}} - l_{\mathrm{n}}\cos(2\theta)\,\alpha_{\mathrm{n}}/3 \end{cases} \tag{16}$$

2.3.3 Equilibrium conditions

From the equilibrium conditions of horizontal forces, vertical forces, and moments of the tenon, the following Equations (17)-(18) can be derived according to the force analysis under clockwise and anti-clockwise rotation shown in Figure 2(a) and (b), respectively.

$$\begin{cases} F_{\mathrm{n}} + T_{\mathrm{b2}} - T_{\mathrm{t1}} - T_{\mathrm{t2}} = 0 \\ F_{\mathrm{t1}} + F_{\mathrm{t2}} - F_{\mathrm{b2}} - T_{\mathrm{n}} = 0 \\ M^{+}(\theta) = F_{\mathrm{t1}}X_{\mathrm{t1}} + F_{\mathrm{t2}}X_{\mathrm{t2}} - F_{\mathrm{b2}}X_{\mathrm{b2}} + F_{\mathrm{n}}X_{\mathrm{n}} + T_{\mathrm{b2}}h_1 + T_{\mathrm{t2}}(h_2 - h_1) \end{cases} \tag{17}$$

$$\begin{cases} F_{\mathrm{h}} + F_{\mathrm{n}} + T_{\mathrm{t2}} - T_{\mathrm{b1}} = 0 \\ F_{\mathrm{b1}} - F_{\mathrm{t2}} + T_{\mathrm{h}} - T_{\mathrm{n}} = 0 \\ M^{-}(\theta) = F_{\mathrm{b1}}X_{\mathrm{b1}} - F_{\mathrm{t2}}X_{\mathrm{t2}} + F_{\mathrm{h}}X_{\mathrm{h}} + F_{\mathrm{n}}X_{\mathrm{n}} + T_{\mathrm{b1}}h_1 + T_{\mathrm{t2}}\left(h_2 - h_1\right) + T_{\mathrm{h}}l_2 \end{cases} \tag{18}$$

Finally, by organizing Equations (1)-(18) according to the flowchart in Figure 4, the M-θ relationship of the PMJs can be obtained numerically.

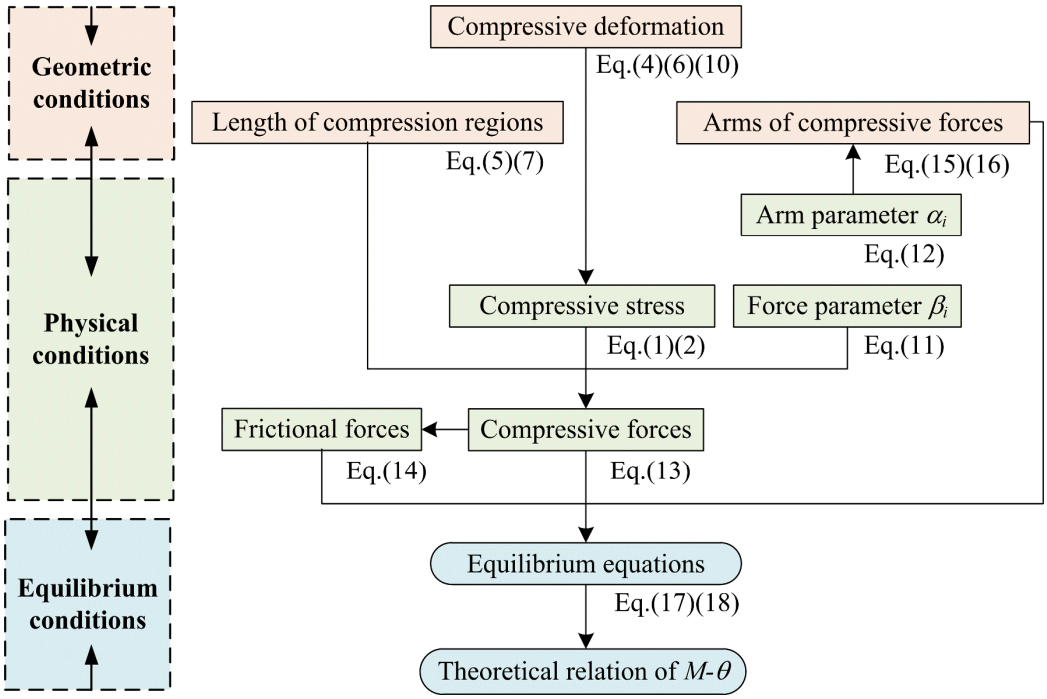

Figure 4. Flowchart for the calculation of the theoretical model

2.4 Verification of the theoretical model

To validate the theoretical model, experimental data about the PMJ specimens in Chun et al. (2016) and Xu et al. (2018) are collected, which is included in Table 1. The theoretical prediction about the rotational behavior of these PMJ specimens was obtained according to the aforementioned analytical procedures.

Besides the experimental results, solid finite element models of the PMJ specimens were also established by ABAQUS software to validate the proposed theoretical model. The geometric and material parameters were referred to the experimental information shown in Table 1. Here, $E_{c,L}$ and $f_{c,L}$ are the elastic modulus and compressive strength along the grain. Then, v_1 and v_2 are the Poisson ratios along and across the grain, respectively. Timber was modeled as orthotropic and elastoplastic material. The Hill yield criterion was chosen to consider the anisotropic plastic behavior of timber.

The interaction between the tenon and the mortise was modeled as hard contact in the normal direction and stiffness penalty in the tangential direction. This means interfaces can transfer pressure and frictional force but not tension. In this simulation, the fiction coefficient took the value of 0.35 in the reasonable range according to relevant literature (McKenzie and Karpovich, 1968; Chen, 2011). The difference between dynamic and static friction coefficients was ignored due to the slow loading process.

Considering the great difference of the elastic modulus along and across the grain, the compressive deformation between the mortise and tenon is considered to take place across the grain. The stiffer mortise acted as the master surface with the coarser mesh while the softer tenon was taken as the slave surface with the denser mesh. The final mesh size was chosen to be 20 mm for the mortise and 10 mm for the tenon. The element type is C3D8R. Figure 5 shows the finite element models of the above PMJ specimens.

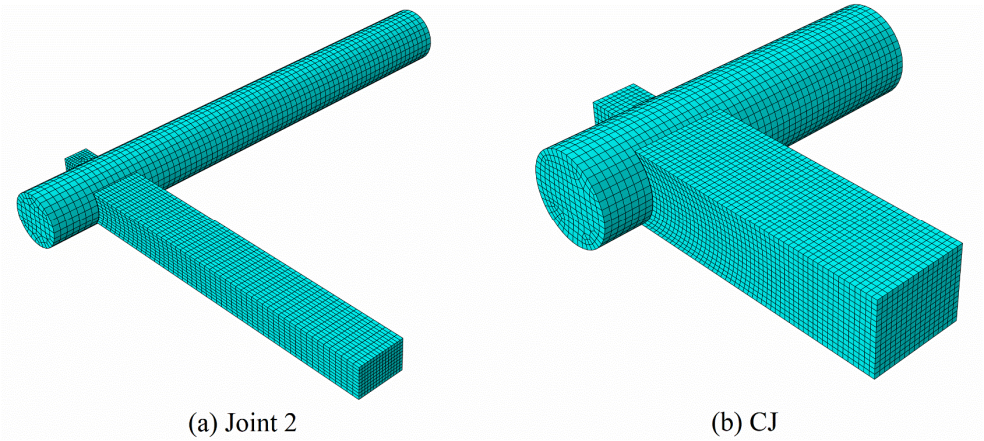

(a) Joint 2 (b) CJ

Figure 5. Solid finite element models of PMJ specimens

Comparisons between the theoretical, simulated and experimental moment-rotation relationship curves are shown in Figure 6. For specimen Joint 2, initial slips in the early stage can be observed in both the theoretical and simulated curves, and these are the results of insufficient contact between the mortise and the tenon due to the initial gaps. The reason why the initial slip is not obvious for the experimental curve may be that the initial gap was closed due to the weight of the wooden beam.

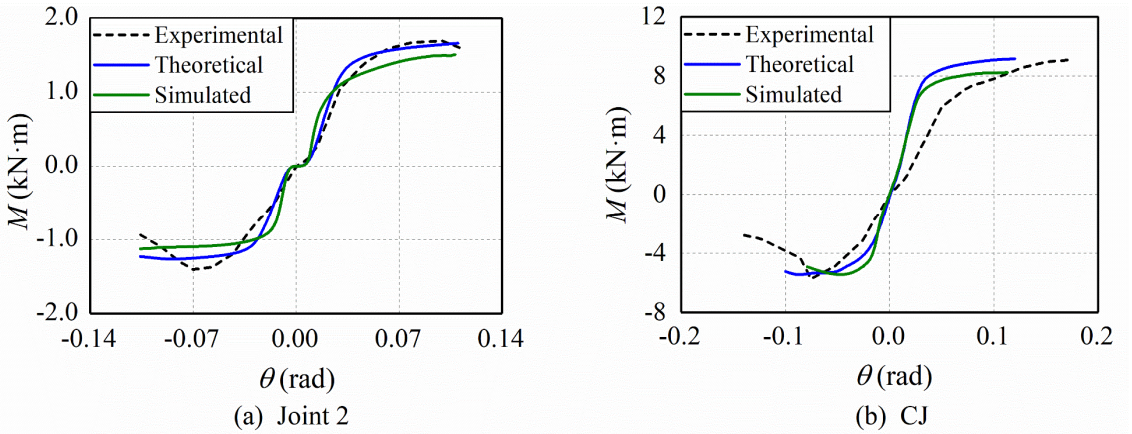

Figure 6. Comparisons between the theoretical, simulated and experimental results

For specimen CJ, the initial rotational stiffness of the theoretical and FE model is larger than that measured in the experiment. It should be noted that the theoretical and FE model of specimen CJ were assumed to be tight as the gap data was not available from the original experimental studies. But actually, inevitable imperfections in the contacting surfaces exist in the specimens due to workmanship in the fabrication process, so this may be the main reason that caused the difference in rotational stiffness. Furthermore, some other experimental studies (Chang et al., 2006; Xue et al., 2020) that found looseness has important effects on the rotational stiffness of PMJs also support the above analysis.

For both specimens, the experimental curves show declining segments under clockwise rotation, but the theoretical and FE models can not reflect this feature. This is because these two models do not take failure modes and the related strength degradation into account due to the complexity of the failure mechanism and material characteristics of PMJs. It remains to be explored in future research work. Despite this, it is acceptable for the preliminary structural analysis because the elastic stiffness and peak moment resistance, the two most important characteristics, have been accurately captured by the theoretical models. Overall, the theoretically predicted moment-rotation relationship shows agreement with the simulated and experimental results, especially the former one,

demonstrating the validity of the theoretical model proposed.

3. Discussion

In this section, the importance of addressing the movement of the rotation center and the bending deformation when dealing with PMJs was carefully investigated. Resistance contributions and elastoplastic states of compression regions were also further analyzed for the subsequent simplification of the theoretical model. The specimen tested by Chun et al. (2016) was employed as the representative example for the discussion.

3.1 Movement of rotation center

As recognized by other studies (Ma et al., 2020; Zhang et al., 2018), the compressive deformation of the tenon mainly depends on the rigid-body motion of the joint. Therefore, the position of the rotation center is of great importance to the distribution of compressive deformation in local regions.

The previous studies have assumed that the rotation center of the PMJ is located at different positions, for instance, at the centroid (Ma et al., 2020; Zhang et al., 2018) or at the interface between the small and larger tenon (He et al., 2021; Pan et al., 2015). These assumptions are generally simple approximations and lack of sound theoretical basis. In this study, with the help of three displacement variables, i.e. u_x, u_y and θ, expressing the rigid-body displacement of the tenon, the position of the rotation center (O_r) can be obtained precisely in accordance with the geometric conditions illustrated in Figure 7(a).

$$\begin{cases} x_{O_r} = u_x - O'O_r \sin\alpha = u_x - u_y/\theta \\ y_{O_r} = u_y + O'O_r \cos\alpha = u_y + u_x/\theta \end{cases} \tag{19}$$

Figure 7(b)(c) shows the horizontal and vertical displacements of the tenon obtained from the theoretical model. Both these two displacements have an

approximately linear relationship with the rotation angle. Unlike dovetail joints (Chen et al., 2016; Li et al., 2016), the horizontal displacement of PMJs appears smaller than the vertical displacement after the early stage, which is consistent with the fact that the failure mode of PMJs is not dominated by the tenon pull-out. This can be explained by the relatively larger moment resistance of PMJs that causes considerable compressive deformation in the vertical contact surfaces between the mortise and the tenon. Besides, the PMJ has certain tensile resistance that also reduces the horizontal displacement of the tenon.

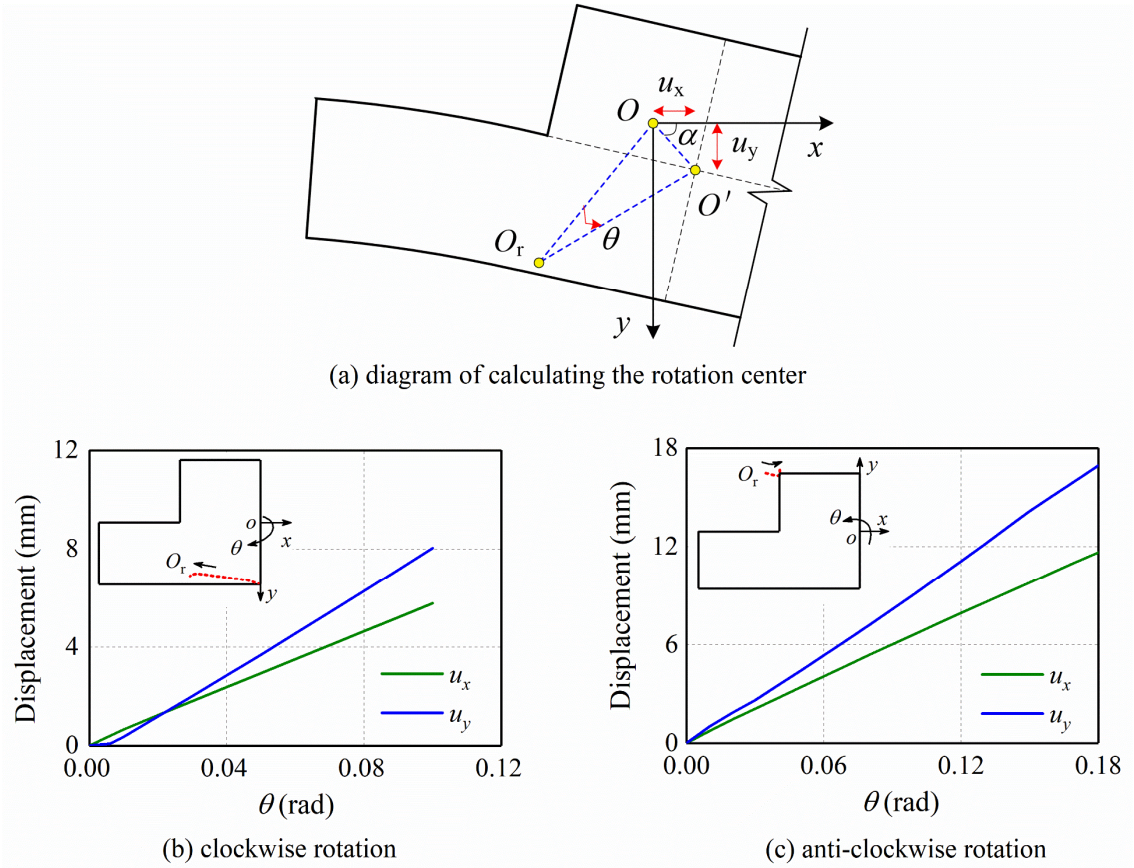

(a) diagram of calculating the rotation center

(b) clockwise rotation

(c) anti-clockwise rotation

Figure 7. Displacements of the tenon and movement of the rotation center

Taking the two displacements obtained above into Equation (19), the movement of the rotation center was calculated and then plotted with red dashed lines in the upper left corner of Figure 7(b)(c). When the PMJ rotates in clockwise and anti-clockwise directions, the rotation center mainly moves around the bottom surface and top surface of

the larger tenon, respectively. Specifically, under clockwise rotation, as shown in Figure 7(b), the rotation center is located at the bottom surface of the tenon neck in the early stage and then gradually moves outward until the interface between the smaller and larger tenon. When rotating anti-clockwise in Figure 7(c), the position of the rotation center is around the front end of the larger tenon. It can be found that the moving range of the rotation center is quite small in the vertical direction but relatively large in the horizontal direction.

Based on the above observation, it is considered that the previous assumption about a fixed rotation center of the tenon is only a simple approximation and is quite inaccurate. The results also confirm the hypothesis made by Tanahashi and Suzuki (2012) that the rotation center of the tenon is not necessarily at the centroid and may move according to the balance of the load and reactions. Therefore, it is necessary to take the movement of the rotation center into consideration for the more accurate calculation of the compression deformation of various local regions.

3.2 Effect of bending deformation

As mentioned earlier, the bending deformation of the smaller tenon may account for a considerable portion of all its deformation due to the relatively large span-depth ratio. Differing from the previous studies (He et al., 2021; Pan et al., 2015; Zhang et al., 2018), the effect of bending deformation is addressed in this paper.

The influence of the bending deformation on the compressive deformation of the smaller tenon is illustrated in Figure 8. The green lines represent the compressive deformation caused by the rigid-body motion only, while the blue lines represent the practical compressive deformation involving the bending deformation. It can be seen clearly that the compressive deformation of the smaller tenon declines greatly after

considering the bending deformation. For example, after involving the bending deformation the maximum compressive deformation under clockwise rotation has dropped from 8.6 mm to 5.8 mm as shown in Figure 8(a).

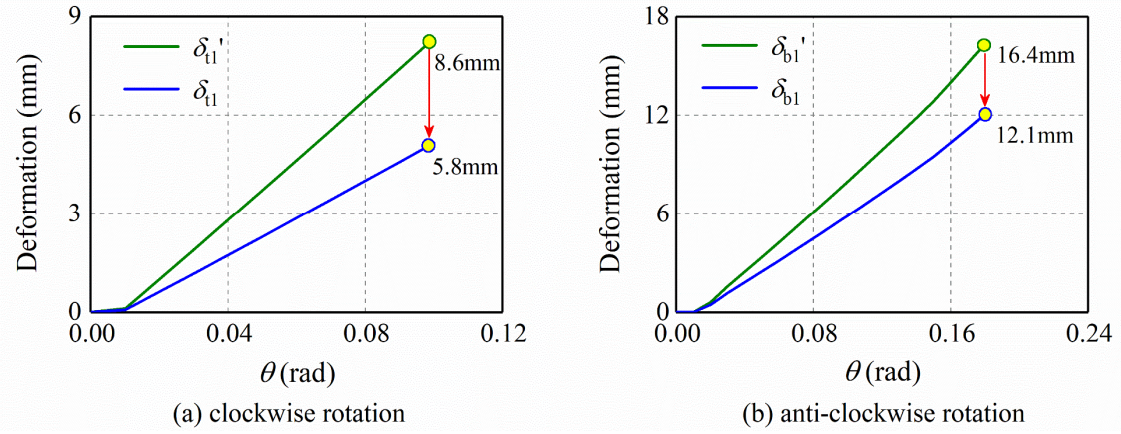

Figure 8. Effect of bending on the compressive deformation of the smaller tenon

According to the principle of deformation compatibility, the theoretical prediction for the compressive deformation of the smaller tenon involving the bending deformation has been obtained by Equation (10). This formula implies the theoretical ratio of compressive deformation without and with considering the bending deformation ($1+\lambda E_{c,R}l^4/(k_iEh^4)$) is closely related to the span-depth ratio of the tenon. In accordance with the theoretical model derived, the proportion of bending deformation of related PMJs in relevant literature has been calculated and the results are included in Table S2.

For most specimens collected here, the bending deformation of the smaller tenon accounts for more than 20% of the compressive deformation caused by the rigid-body motion while that of the larger tenon is generally lower than 5%. Hence, it can be concluded that the bending deformation of the larger tenon is quite small but that of the smaller tenon is relatively large for most cases. It is necessary to consider the bending deformation of the smaller tenon when analyzing the rotational behavior of PMJs.

3.3 Resistance contributions of compression regions

Resisting moments produced by individual compression regions of PMJs can be

calculated and then their contributions to the resistance of the joint are obtained. It is found that the smaller tenon plays a remarkable role in resisting external loads. Specifically, the top and bottom surfaces of the smaller tenon, i.e. region-t_1 and region-b_1, produce the main resisting moments while the contributions from the top and front surfaces of the larger tenon, i.e. region-t_2 and region-h, are negligible under clockwise and anti-clockwise rotation respectively.

Since the smaller tenon accounts for the largest moment proportion, the elastoplastic state of its compression regions is considered to affect the development of the whole resisting moment directly. The ratio of the compressive deformation when wood yields to the practical compressive deformation, i.e. $\delta_{y,i}/\delta_i$, can be taken as an indicator to reflect the development of the plastic zone in the smaller tenon. Figure 9 shows the relationship between the indicator and the moment of the PMJ. It is observed that the inflection points of these two curves appear almost at the same rotation angle. When the value of $\delta_{y,i}/\delta_i$ declines to 0.05, the curves of M-θ approximately reach equivalent yield points, i.e. points A and B shown in Figure 9. Furthermore, the resistance of the joint reaches the peak moment with the value of $\delta_{y,i}/\delta_i$ approaching zero, which indicates that the corresponding compression region of the smaller tenon has completely yielded.

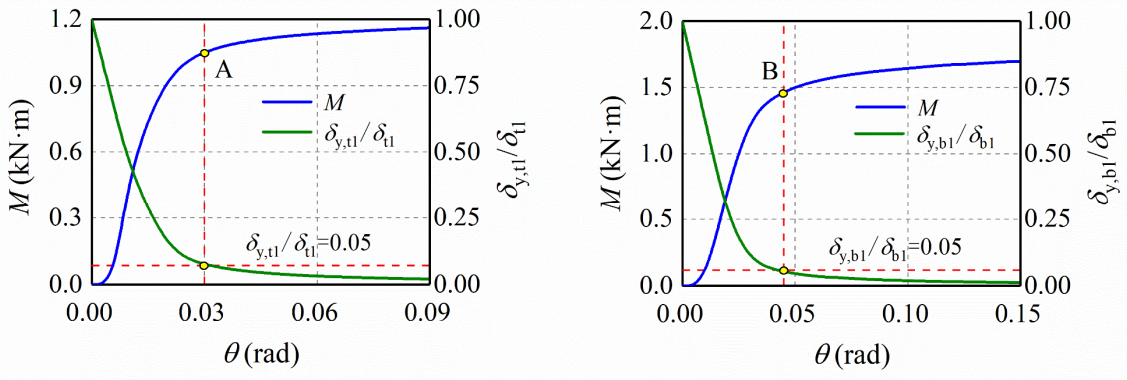

(a) clockwise rotation (b) anti-clockwise rotation

Figure 9. Relationship between the indicator $\delta_{y,i}/\delta_i$ and the theoretical moment

4. Simplification of the theoretical model

The theoretical model proposed can be used to predict the moment-rotation curves of PMJs through a numerical procedure. However, in many cases, the stiffness and peak moment of the joints are of primary interest in design applications. Based on the above analysis, the contributions from region-t_2 and region-h can be negligible under clockwise and anti-clockwise rotation, respectively. Therefore, the total resistance can be simplified as:

$$\begin{cases} M^{+}(\theta) = M_{\mathrm{t_1}} + M_{\mathrm{b_2}} + M_{\mathrm{n}} = F_{\mathrm{t_1}} X_{\mathrm{t_1}} - F_{\mathrm{b_2}} X_{\mathrm{b_2}} + F_{\mathrm{n}} X_{\mathrm{n}} \\ M^{-}(\theta) = M_{\mathrm{b_1}} + M_{\mathrm{t_2}} + M_{\mathrm{n}} = F_{\mathrm{b_1}} X_{\mathrm{b_1}} + T_{\mathrm{b_1}} h_1 - F_{\mathrm{t_2}} X_{\mathrm{t_2}} + F_{\mathrm{n}} X_{\mathrm{n}} \end{cases} \tag{20}$$

4.1 Simplified calculation formulas

4.1.1 Equivalent elastic stiffness

It is assumed that the moment-rotation curve reaches the equivalent yield point when the indicator $\delta_{\mathrm{y,i}}/\delta_{\mathrm{l}}$ approaches 0.05. By organizing Equations (2) and (10), the rotation angle at the equivalent yield point can be expressed as

$$\begin{cases} \theta_{\mathrm{y}}^{+} = \dfrac{5h_1 f_{\mathrm{c,R}}}{l_1 E_{\mathrm{c.R}}}\left(1 + \dfrac{6E_{\mathrm{c.R}} l_1^{4}}{E h_1^{4}}\right) + \theta_0^{+} \\ \theta_{\mathrm{y}}^{-} = \dfrac{5h_1 f_{\mathrm{c,R}}}{(D - 1.25l_2) E_{\mathrm{c.R}}}\left(1 + \dfrac{6E_{\mathrm{c.R}} l_1^{4}}{E h_1^{4}}\right) + \theta_0^{-} \end{cases} \tag{21}$$

In the simplified calculation, it should be noted that the horizontal and vertical displacements of the tenon are treated as linear functions of the rotation angle according to the analysis in the above section. Besides, trigonometric functions of rotation angle can also be simplified as finite polynomial functions by Taylor series expansion since the rotation angle of the PMJ is generally small.

By substituting Equation (21) into Equation (20) and organizing Equations (13)-(18), the resisting moment at the equivalent yield point can be obtained as:

$$\begin{cases} M_{\mathrm{y}}^{+}=M^{+}(\theta)\Big|_{\theta=\theta_{\mathrm{y}}^{+}}=0.95 f_{\mathrm{c,R}} b l_{\mathrm{t1}}\left[D-0.5 l_{\mathrm{t1}}+\mu X_{\mathrm{n}}^{+}-\left(1-\mu^{2}\right) X_{\mathrm{b2}}^{+}\right]\Big|_{\theta=\theta_{\mathrm{y}}^{+}} \\ M_{\mathrm{y}}^{-}=M^{-}(\theta)\Big|_{\theta=\theta_{\mathrm{y}}^{-}}=0.95 f_{\mathrm{c,R}} b l_{\mathrm{b1}}\left[D-0.5 l_{\mathrm{b1}}+\mu\left(h_{1}+X_{\mathrm{n}}^{-}\right)-\left(1-\mu^{2}\right) X_{\mathrm{t2}}^{-}\right]\Big|_{\theta=\theta_{\mathrm{y}}^{-}} \end{cases} \tag{22}$$

where l_{i} and X_{i} represent the compression length and the lever arm of region-i, respectively. Based on Equations (6)(8)(15)(16), the compression length and the lever arms involved in Equation (22) can be simplified as:

$$\begin{cases} l_{\mathrm{t1}}=l_{1}+0.4 h_{2} \theta-\left(h_{01}-l_{2} \theta_{0}^{+}\right) / \theta \\ X_{\mathrm{n}}^{+}=0.5 h_{1}+0.2 h_{2}+l_{2}\left(\theta-\theta_{0}^{+}\right) \\ X_{\mathrm{b2}}^{+}=0.5 l_{2}+\left(0.25 h_{1}-0.2 h_{2}\right) \theta-0.5 l_{2} \theta_{0}^{+} / \theta \\ l_{\mathrm{b1}}=D-1.25 l_{2}+(0.5 h_{1}+0.425 h_{2}) \theta-\left(h_{0}-1.25 l_{2} \theta_{0}^{-}\right) / \theta \\ X_{\mathrm{n}}^{-}=0.7125 h_{2}-0.5 h_{1}+1.25 l_{2}\left(\theta-\theta_{0}^{-}\right) \\ X_{\mathrm{t2}}^{-}=0.625 l_{2}+\left(0.0375 h_{2}-0.25 h_{1}\right) \theta-\left(0.625 l_{2} \theta_{0}^{-}+0.5 h_{02}\right) / \theta \end{cases} \tag{23}$$

Based on the rotation angle and resisting moment at the equivalent yield point, the equivalent elastic stiffness can be expressed as

$$\begin{cases} K^{+}=\dfrac{M_{\mathrm{y}}^{+}}{\theta_{\mathrm{y}}^{+}}=\dfrac{0.95 f_{\mathrm{c,R}} b l_{\mathrm{t1}}\left[D-0.5 l_{\mathrm{t1}}+\mu X_{\mathrm{n}}^{+}-\left(1-\mu^{2}\right) X_{\mathrm{b2}}^{+}\right]}{\dfrac{5 h_{1} f_{\mathrm{c,R}}}{l_{1} E_{\mathrm{c.R}}}\left(1+\dfrac{6 E_{\mathrm{c.R}} l_{1}^{4}}{E h_{1}^{4}}\right)+\theta_{0}^{+}}\Bigg|_{\theta=\theta_{\mathrm{y}}^{+}} \\ K^{-}=\dfrac{M_{\mathrm{y}}^{-}}{\theta_{\mathrm{y}}^{-}}=\dfrac{0.95 f_{\mathrm{c,R}} b l_{\mathrm{b1}}\left[D-0.5 l_{\mathrm{b1}}+\mu\left(h_{1}+X_{\mathrm{n}}^{-}\right)-\left(1-\mu^{2}\right) X_{\mathrm{t2}}^{-}\right]}{\dfrac{5 h_{1} f_{\mathrm{c,R}}}{(D-1.25 l_{2}) E_{\mathrm{c.R}}}\left(1+\dfrac{6 E_{\mathrm{c.R}} l_{1}^{4}}{E h_{1}^{4}}\right)+\theta_{0}^{-}}\Bigg|_{\theta=\theta_{\mathrm{y}}^{-}} \end{cases} \tag{24}$$

4.1.2 Peak moment

According to the analysis in Section 3.3, the compression regions of the smaller tenon

have completely yielded when the moment-rotation curves reach peak points. In other words, the compression deformation of the root segment of the smaller tenon equals the deformation required for wood yielding. By organizing Equations (2)(5)(7), the peak rotation angle can be obtained as follows.

$$\begin{cases} \theta_{\mathrm{p}}^{+} = \sqrt{\dfrac{5\left(h_{01} - l_2\theta_0^{+}\right)}{2h_2} + \dfrac{5h_1 f_{\mathrm{c,R}}}{8h_2 E_{\mathrm{c.R}}}} \\ \theta_{\mathrm{p}}^{-} = \dfrac{l_2 + \sqrt{{l_2}^2 - (8h_1 + 6.8h_2)(5l_2\theta_0^{-} - 4h_0 - h_1 f_{\mathrm{c,R}} / E_{\mathrm{c.R}})}}{4h_1 + 3.4h_2} \end{cases} \tag{25}$$

By substituting Equation (25) into Equation (20) and organizing Equations (13)-(18), the moment at the peak point can be expressed as:

$$\begin{cases} M_p^{+} = M^{+}(\theta)\Big|_{\theta=\theta_p^{+}} = f_{\mathrm{c,R}} b l_1 \left[D - 0.5l_1 + \mu X_{\mathrm{n}}^{+} - \left(1-\mu^2\right) X_{\mathrm{b2}}^{+} \right]\Big|_{\theta=\theta_{\mathrm{p}}^{+}} \\ M_{\mathrm{p}}^{-} = M^{-}(\theta)\Big|_{\theta=\theta_{\mathrm{p}}^{-}} = f_{\mathrm{c,R}} b l_1 \left[D - 0.5l_1 + \mu\left(h_1 + X_{\mathrm{n}}^{-}\right) - \left(1-\mu^2\right) X_{\mathrm{t2}}^{-} \right]\Big|_{\theta=\theta_{\mathrm{p}}^{-}} \end{cases} \tag{26}$$

4.2 Verification of simplified calculation formulas

To validate the simplified calculation method, more experimental data about the flexural behavior of PMJs were collected from relevant studies in the existing literature. Table 2 summarizes the geometric and material parameters of the specimens collected. It is noteworthy that some input parameters that are required for the simplified calculation are not available from the original experimental studies, and these are estimated based on reasonable deductions. Specifically, the missing data in part of the material properties and the initial gaps are estimated in accordance with the information by Long and Yang (2005) and Yang et al. (2020).

Comparisons between the equivalent elastic stiffness and peak moment predicted from the simplified calculation and those determined from the experiments, are shown in

Figure 10. It can be observed that the predictions of the simplified calculations correspond well with the experimental results, demonstrating the validity of the theoretical model proposed and the adequacy of the simplified formulas.

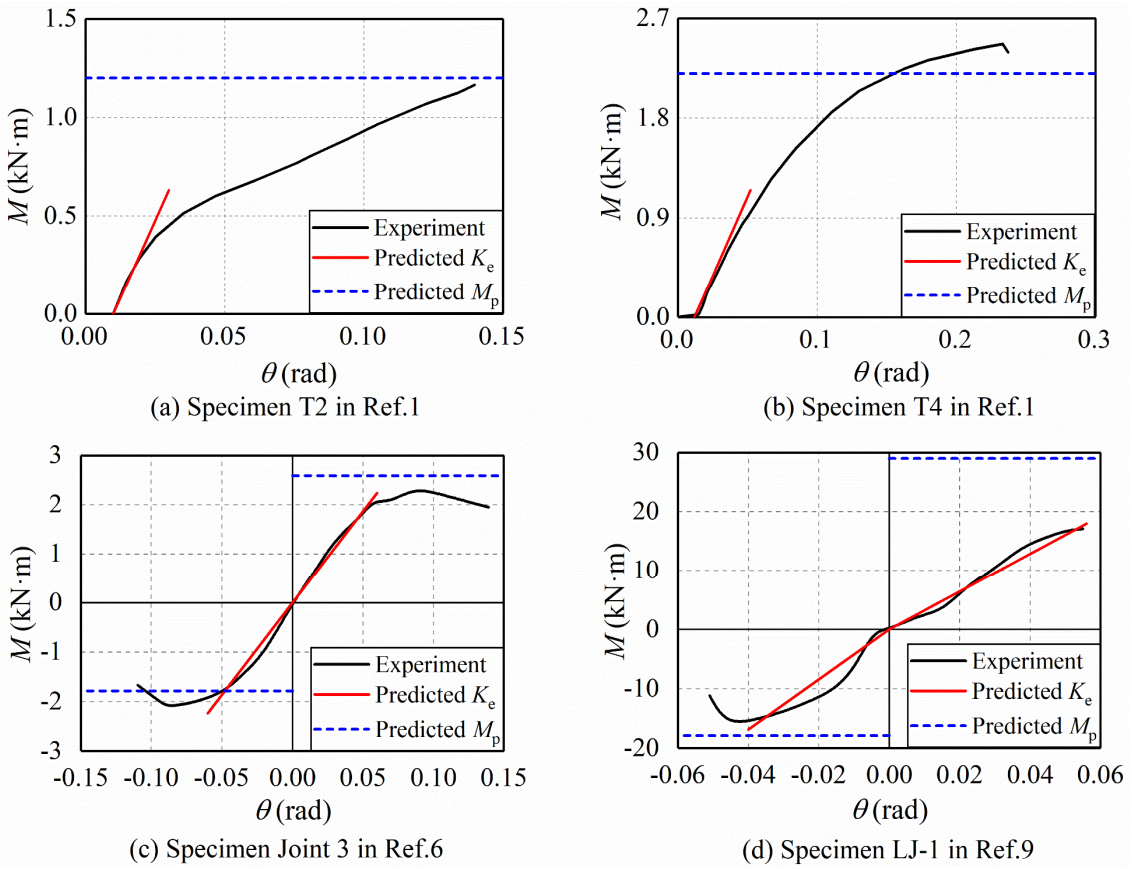

Figure 10. Comparisons between the predicted stiffness, peak moment and test curves

In order to further validate the proposed model, the equivalent stiffness and peak moment of all specimens summarized in Table 2 are calculated and then compared with the experimental results. Detailed data are included in Table S3 of the supplemental material. It should be noted that the experimental stiffness of some specimens is not available directly from the original experimental data and in such cases, Park's method (Park and Paulay, 1975) is used to determine the experimental stiffness.

Figure 11(a)(b) shows the comparison of the predicted equivalent stiffness ($K_{e,c}$) and the experimental results ($K_{e,e}$). The average ratio ($K_{e,c}/K_{e,e}$) is 1.06 with a coefficient of variation (COV) of 0.28. The comparison of the peak moment is shown in Figure

11(c)(d), where the average ratio ($M_{p,c}/M_{p,e}$) is found to be 1.09 and the COV is 0.25. From Figure 11, it can be seen that relatively large errors occur in a small portion of the test specimens. This may be explained by two main reasons. One is that some cyclic loading tests ended with failure under clockwise rotation (He, 2019), which resulted in lower ultimate moment values under anti-clockwise rotation. This is the main reason why a large number of data points in Figure 11(d) are larger than unity. Another is that there are inevitable variations in the experimental results because of the complexity of the geometric features and material properties of PMJs. For instance, considerable variations of the experimental stiffness of specimens can be found in Zhao et al. (2010), even though all joints in the test were made of the same batch of wood and designed to be the same size. Overall, it can be seen from Figure 11 that the simplified predictions are satisfactory.

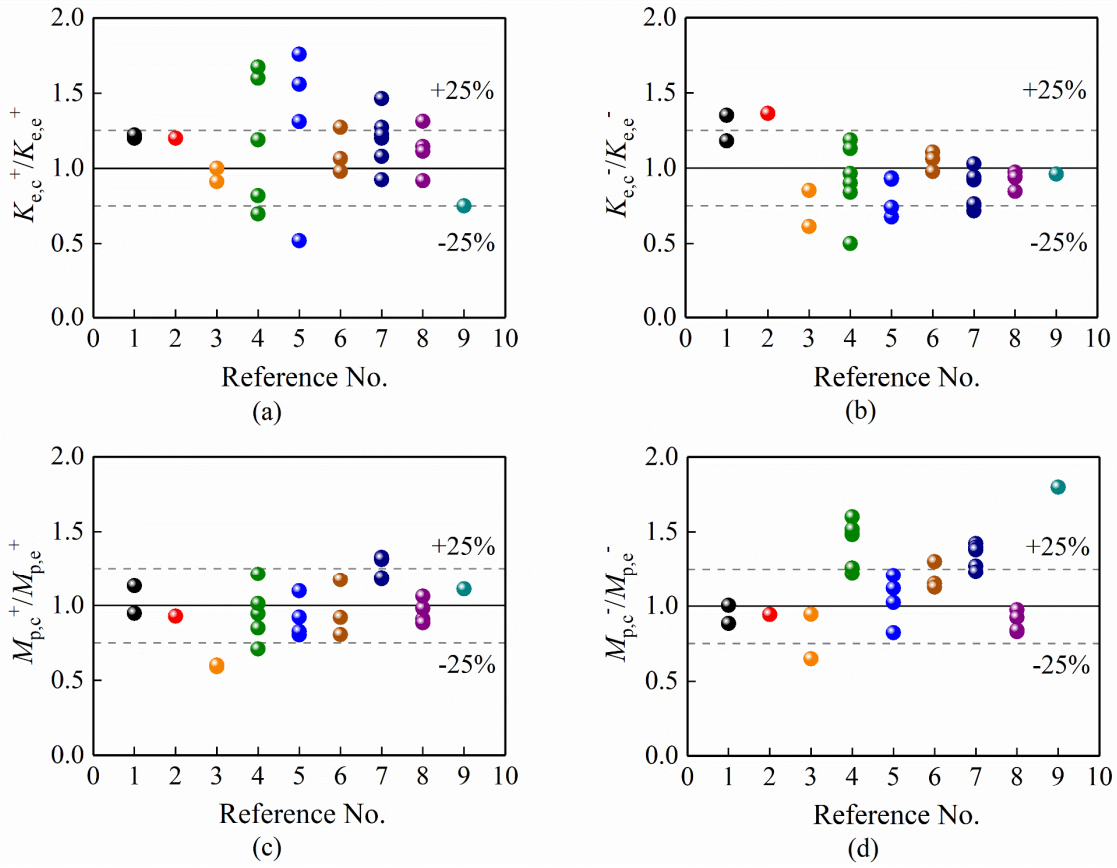

Figure 11. Comparison between predicted and experimental results of stiffness and peak moment for all collected specimens

5. Application of the theoretical model

5.1 Test specimens

To verify the applicability of the theoretical model proposed, it is necessary to investigate the lateral responses of timber frames connected by PMJs. The experimental results of three 1:3.52 scaled single-story and single-bay timber frames tested by Sui (2009) were chosen as a reference. These specimens were fabricated according to the traditional methods recorded in "Yingzao Fashi" which is the first official Chinese treatise on architecture and craftsmanship (Pan and He, 2005). Each frame consisted of a main beam and two round columns, whose configuration and dimensions are shown in Figure 12(a).

The vertical load of 10 kN was applied on each column to simulate the actual upper load supported by frames. The column foot joints were set as the fixed hinge bearing in the test. The timber members were made of Pinus koraiensis and the material properties are as follows: MOE along and across the grain are 10110 MPa and 654 MPa, respectively; compressive strength along and across the grain are 34.76 MPa and 3.6 Mpa, respectively.

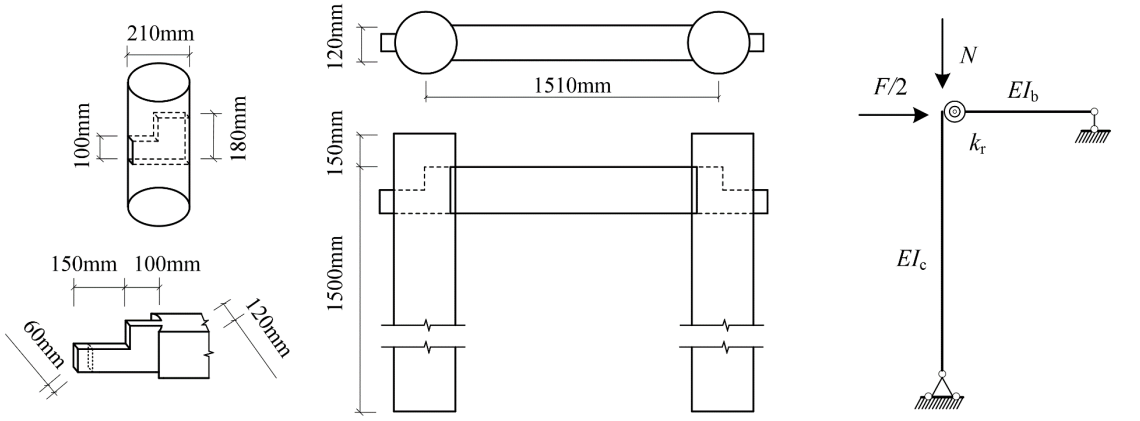

(a) Configuration and dimensions of the timber frame (b) schematic diagram for calculation

Figure 12. Sketch of timber frames and schematic diagram for calculation

5.2 Lateral stiffness of timber frame

As an important performance index, lateral stiffness plays a dominant role in structural

deformability and dynamic characteristics. For timber frames without walls, it depends mainly on the rotational stiffness of the semi-rigid mortise-tenon joints and the column-foot joint, and the flexural stiffness of the timber members (Suzuki and Maeno, 2006). Since the above specimens were set on the fixed hinge bearing, the stiffness contribution from the column-foot joint can be neglected approximately.

Considering the symmetry of the structure and the force conditions, the whole frame can be simplified as the half structure for analysis, as shown in Figure 12(b). It should be noted that although PMJs show asymmetric features under clockwise and anticlockwise rotation, the lateral stiffness of the frame remains consistent because the PMJs are usually used in pairs. Due to this, the rotational stiffness of beam-column joints k_r can take the average value of the equivalent elastic stiffness of PMJs under clockwise and anticlockwise rotation. The relationship between k_r and the line rigidity of the beam and column (i_b, i_c) is substituted by $\kappa = i_b/i_c$ and $\eta = i_b/k_r$. The rotation angle and the horizontal displacement of the frame are represented by θ and Δ, respectively. The stiffness equation for the timber frame can be expressed as

$$\begin{bmatrix} k_{11} & k_{12} \\ k_{21} & k_{22} \end{bmatrix} \begin{bmatrix} \theta \\ \Delta \end{bmatrix} = \begin{bmatrix} 0 \\ F/2 \end{bmatrix} \tag{27}$$

where

$$k_{11} = 3i_c + \frac{6i_b}{1+\frac{6i_b}{k_r}} = 3i_c\left(1+\frac{2\kappa}{1+6\eta}\right);\ k_{22} = \frac{3i_c}{H^2};\ k_{12} = k_{21} = \frac{-3i_c}{H}$$

On this base, the relationship between the lateral force and displacement can be expressed as

$$F = 2\left(k_{22} - \frac{k_{12}k_{21}}{k_{11}}\right)\Delta = \frac{6i_c}{H^2}\frac{2\kappa}{1+2\kappa+6\eta}\Delta \tag{28}$$

The lateral stiffness of the timber frame can finally be obtained as

$$D_{\mathrm{f}} = \frac{6i_{\mathrm{c}}}{H^2}\frac{2\kappa}{1+2\kappa+6\eta} \tag{29}$$

5.3 Verification of the lateral stiffness

To verify the lateral stiffness given by Equation (29), the rotational stiffness of PMJs needs to be calculated first. According to Equations (21)(22)(25)(26), the equivalent yield point and peak point of the simplified mechanical model for PMJs can be obtained. Meanwhile, the equivalent elastic stiffness can also be determined from Equation (24). The simplified theoretical model was compared with the M-θ skeleton curves of PMJs obtained from the test by Sui (2009), as shown in Figure 13 (a).

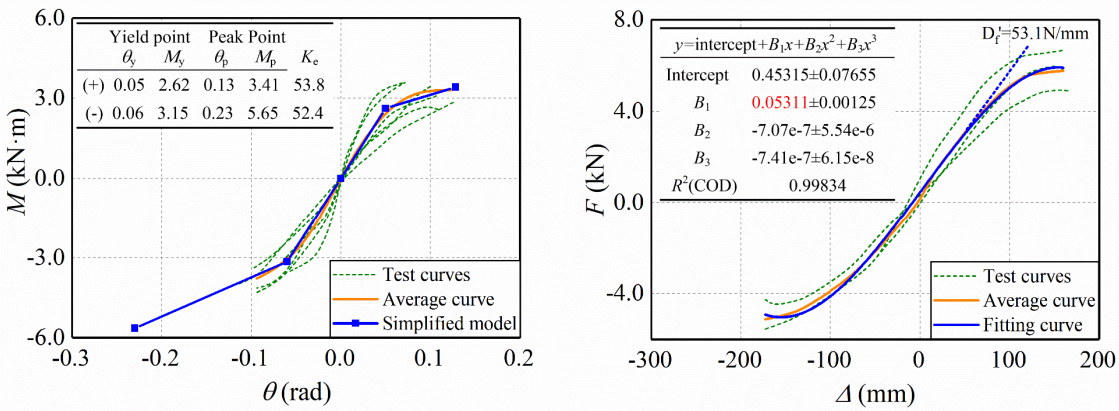

(a) Comparison between simplified model and test curves (b) Experimental lateral stiffness of the frame

Figure 13. Simplified model of PMJs and experimental lateral stiffness of timber frames

It can be found that the simplified model matches well with the average experimental curve, demonstrating again the validity of the theoretical model. After obtaining the rotational stiffness of the PMJ, the lateral stiffness of the timber frame can be calculated according to Equation (29), with a theoretical estimation of 50.9 N/mm.

To obtain the experimental value of the lateral stiffness, the average curve was obtained based on the F-Δ skeleton curves of three timber frames tested. Then, the average curve was processed by the method of polynomial fitting. The first-order

coefficient of the fitting curve is just equal to the experimental value of the lateral stiffness, i.e. 53.1 N/mm, as illustrated in Figure 13 (b). Comparing the theoretical estimation with the experimental stiffness, the relative error is only (50.9-53.1)/53.1=-4.2%, which is pretty acceptable. This indicates that the proposed theoretical model and the corresponding simplified calculation formulas are of a certain accuracy and can be applied to the calculation of the lateral stiffness of timber frames.

6. Conclusion

An improved theoretical model for predicting the rotational behavior of penetrated mortise-tenon joints was proposed in this paper. In contrast to the previous models, the model presented herein is unique and more comprehensive in that it introduces three displacement variables to describe the rigid-body motion of the tenon without presuming the rotation center in advance, and considers the bending deformation for more accurate calculation of the compressive deformation of the tenon. Based upon the theoretical model, simplified calculation methods for equivalent elastic stiffness and peak moment of PMJs were proposed and then applied for the calculation of the lateral stiffness of timber frames. A wide range of available experimental data on PMJs and timber frames connected by PMJs were collected from the existing literature. Good agreement was found from the comparison of the predicted and experimental results, demonstrating the validity of the estimation method derived and its applicability to the structural analysis.

In addition to the estimation for the rotational behavior, new insight into the internal mechanism of PMJs regarding the rotation center and bending deformation has been gained from the quantitive analysis by the theoretical model. Specifically, the rotation center of the tenon is not stationary, moving around the bottom and top surface of the larger tenon under clockwise and anti-clockwise rotation respectively. This finding confirms the previous hypothesis that the rotation center of the tenon is not necessarily at

the centroid and may move according to the balance of the load and reactions (Tanahashi and Suzuki, 2012). The work also reveals the significance of the bending effect in evaluating the deformation of PMJs. For the traditional configuration of PMJs, the bending deformation causes a reduction of at least 20% in the compressive deformation of the smaller tenon due to its relatively large span-depth ratio, and hence lowers the moment resistance of PMJs. Therefore, it is necessary to consider the effect of the bending deformation of the smaller tenon when dealing with the rotational behavior of PMJs.

Acknowledgements

This work was supported by the Thirteenth Five-Year National Key Research and Development Program of China under Grant No. 2017YFC0703503.

Disclosure

The authors declare that there are no conflicting interests that could have appeared to influence the work reported in this paper.

References

Chang WS and Hsu MF (2007) Rotational performance of traditional Nuki joints with gap II: the behavior of butted Nuki joint and its comparison with continuous Nuki joint. Journal of Wood Science 53(5):401–407. Doi: 10.1007/s10086-007-0880-1.

Chen CC and Qiu HX (2016) Flexural behavior of penetrated mortise-tenon joints (in Chinese). Journal of Southeast University (Natural Science Edition) 46(2): 326-334. Doi: 10.3969/j.issn.1001-0505.2016.02.016.

Chang WS, Hsu MF and Komatsu K (2006) Rotational performance of traditional Nuki joints with gap I: Theory and verification. Journal of Wood Science 52(1):58–62. Doi:10.1007/s10086-005-0734-7.

Chen L, Li SC, Wang Y, et al. (2017) Experimental Study on the Seismic Behaviour of Mortise-Tenon Joints of the Ancient Timbers. Structural Engineering

International 27(4): 512-519. Doi: 10.2749/ 222137917X14881937844720.

Chun Q, Pan JW and Dong YH (2016) Mechanical Properties of Tou Mortise-tenon Joints of the Traditional Timber Buildings in the South Yangtze River Regions (in Chinese). Journal of Southwest Jiaotong University 51(5): 862-869. Doi: 10.3969/j.issn.0258-2724.2016.05.007.

Chen CC, Qiu HX and Lu Y (2016) Flexural behavior of timber dovetail mortise-tenon joints. Construction and Building Materials 112: 366-377. Doi: 10.1016/j.conbuildmat.2016.02.074.

Chen ZY (2011) Behaviour of typical joints and the structure of Yingxian wood pagoda (in Chinese). Ph.D. thesis, Harbin Institute of Technology, Harbin, China.

Eckelman CA and Haviarova V (2008) Rectangular mortise and tenon semirigid joint connection factors. Forest Products Journal 58(12): 49–55.

GB50005-2017 (2017) Standard for design of timber structures (in Chinese). Beijing: China Architecture and Building Press.

Gao YL, Tao Z, Ye LY, et al. (2015) Low-cycle reversed loading tests study on typical mortise-tenon joints of traditional timber building based on friction mechanism (in Chinese). Journal of Building Structures 36(10): 139-145. Doi: 10.14006/j.jzjgxb.2015.10.017.

He JX (2019) Study on Mechanical Properties of Key Joints and Column Frame in Traditional Timber Structure (in Chinese). Ph.D. dissertation, Beijing Jiaotong University, Beijing, China.

He JX, Yu P, Wang J, et al. 2021. Theoretical model of bending moment for the penetrated mortise-tenon joint involving gaps in traditional timber structure. Journal of Building Engineering 42(2021). Doi: 10.1016/j.jobe.2021.103102.

King WS, Yen JY and Yen YN (1996) Joint characteristics of traditional Chinese wooden

frames. Engineering Structures 18(8): 635–44. Doi:10.1016/0141-0296(96)00203-9.

Long WG and Yang XB (2005) Wood design manual (in Chinese). 3rd ed. Beijing: China Architecture and Building Press.

Li YZ, Cao SY and Xue JY (2016) Analysis on mechanical behavior of dovetail mortise-tenon joints with looseness in traditional timber buildings. Structural Engineering and Mechanics 60(5): 903-921. Doi: 10.12989/sem.2016.60.5.903.

Ma BJ (1991) Wooden construction technology of Chinese ancient architecture (in Chinese). Beijing: Science Press.

Ma LL, Xue JY, Dai WQ, et al. (2020) Moment-rotation relationship of mortise-through-tenon connections in historic timber structures. Construction and Building Materials 232(1): 1-10. Doi: 10.1016/j.conbuildmat.2019.117285.

McKenzie WM and Karpovic H (1968) The frictional behaviour of wood. Wood Science and Technology 2:139-152.

Nowak TP, Jasienko J and Czepizak D (2013) Experimental tests and numerical analysis of historic bent timber elements reinforced with CFRP strips. Construction and Building Materials 40: 197-206. Doi: 10.1016/j.conbuildmat.2012.09.106

Ogawa K, Sasaki Y and Yamasaki M (2016) Theoretical estimation of the mechanical performance of traditional mortise–tenon joint involving a gap. Journal of Wood Science 62: 242–250. Doi: 10.1007/s10086-016-1544-9.

Pan GX and He JZ (2005) An interpretation of Ying Zao Fa Shi. Nanjing: Southeast University Press.

Park R and Paulay T (1975) Reinforced Concrete Structures. New York: John Wiley & Sons.

Poletti E, Vasconcelos G, Branco JM, et al. (2019) Effects of extreme environmental

exposure conditions on the mechanical behaviour of traditional carpentry joints. Construction and Building Materials 213: 61-78. Doi: 10.1016/j.conbuildmat. 2019.04.030.

Pan Y, Wang C, Tang LN, et al. (2015) Study on mechanical model of straight-tenon joints in ancient timber structures (in Chinese). Engineering Mechanics 32(2): 82-89. Doi: 10.6052/j.issn.1000-4750.2013.08.0728.

Sui Y (2009) Analysis on Energy Dissipation Mechanism and Dynamic Characteristic for Chinese Ancient Timber Buildings (in Chinese). Ph.D. dissertation, Xi'an University of Architecture and Technology, Xi'an, China.

Suzuki Y and Maeno M (2006) Structural mechanism of traditional wooden frames by dynamic and static tests. Structural Control and Health Monitoring 13: 508–22. Doi: 10.1002/(ISSN)1545-2263.

Seo JM, Choi IK and Lee JR (1999) Static and cyclic behavior of wooden frames with tenon joints under lateral load. Journal of Structural Engineering 125(3): 344-349. Doi: 10.1061/(ASCE)0733-9445 (1999)125:3(344).

Su HH, Gao YL, Tao Z, et al. (2020) Tests for effects of lateral tenon and mortise tightness on aseismic performance of step-through tenon joints (in Chinese). Journal of Vibration and Shock 39(15): 142-149. Doi: 10.13465/j.cnki.jvs.2020.15.019.

Tanahashi H and Suzuki Y (2012) Basic concept and general formulation of restoring force characteristics of traditional wooden joints. Paper presented at Proceedings of the 13th World Conference on Timber Engineering, Auckland, New Zealand, July 16-19.

Xie QF, Wang L, Zheng PJ, et al. (2018) Rotational behavior of degraded traditional mortise-tenon joints: experimental tests and hysteretic model. International Journal of Architectural Heritage 12(1): 125-36. Doi: 10.1080/15583058.

2017.1390629.

Xue JY, Xu D and Xia HL (2020) Experimental Study on Seismic Performance of Through-Tenon Joints with Looseness in Ancient Timber Structures. International Journal of Architectural Heritage 14(4): 483-495. Doi: 10.1080/15583058.2018.1552996.

Xu QF, Zhang FW, Chen X, et al. (2018). Experimental research on strengthening methods for through-mortise and tenon joints of Qing-style timber buildings (in Chinese). Sciences of Conservation and Archaeology 30(4): 70-79. Doi: 10.16334/j.cnki.cn31-1652/k.2018.04.009.

Yang QS, Gao C, Wang J, et al. (2020) Probability distribution of gaps between tenon and mortise of traditional timber structures. European Journal of Wood and Wood Products 78:27-39. Doi: 10.1007/s00107-019-01472-1.

Zhang XC, Dai WQ and Xue JY (2018) Theoretical Analysis on Moment-rotation Relationship of Through tenon Joint with Gap (in Chinese). Journal of Hunan University (Natural Sciences) 45(05): 125-133. Doi: 10.16339/j.cnki.hdxbzkb.2018.05.015.

Zhao HT, Dong CY, Xue JY, et al. (2010) The experimental study on the characteristics of mortise tenon joint historic timber buildings (in Chinese). Journal of Xi'an University of Architecture and Technology (Natural Science Edition) 42(3): 315-318.

Tables with captions

Table 1. Dimensions (unit: mm) and material properties of the experimental joints

Reference	Specimen	D	B	h_1	h_2	l_1	l_2	b	h_{01}	h_{02}
Chun et al. (2016)	Joint 2	170	100	75	150	85	85	40	1	1
Xu et al. (2018)	CJ	260	210	130	260	130	130	70	-	-

Table 1. Continued

Reference	Specimen	species	Density (kg/m^3)	$E_{c,R}$ (MPa)	$E_{c,L}$ (MPa)	E (MPa)	$f_{c,R}$ (MPa)	$f_{c,L}$ (MPa)	v_1	v_2
Chun et al. (2016)	Joint 2	Fir	450	1000	10000	10238	3.0	23.7	0.35	0.1
Xu et al. (2018)	CJ	Pine	596	795	12520	7640	3.3	27.5	0.42	0.02

Table 2. Dimensions and material properties of the experimental joints

Ref.	Specimens	D/mm	B/mm	h/mm		l/mm		b	h_0/mm		$f_{c,R}$	$E_{c,R}$
				h_1	h_2	l_1	l_2	/mm	h_{01}	h_{02}	/MPa	/MPa
1	T1/T2	170	115	75	150	85	85	40	1.5	3	3.3	1018
	T3/T4	170	115	75	150	85	85	40	2.5	2.5	3.3	1018
2	CJ	260	210	130	260	130	130	70	-	-	596	795
3	Pinned 1/2	120	70	55	110	60	60	35	0	0	5.5	-
4	Left/Right No.1/2/3	210	120	100	180	110	100	60	-	-	2.9	900
5	TS0.38	200	140	100	175	100	100	50	-	-	3.7	890
	TS0.20	200	140	100	175	100	100	50	-	-	3.7	890
6	Joint 1/ 2	170	100	75	150	85	85	40	1	1	3.0	1000
	Joint 3	170	100	75	150	85	85	50	1	1	3.0	1000
7	TJ1	240	128	80	160	120	120	60	0	0	3.16	268
	TJ2	240	128	76	156	120	120	60	4	4	3.16	268
	TJ3	240	128	72	152	120	120	60	8	8	3.16	268
	TJ4	240	128	68	148	120	120	60	12	12	3.16	268
	TJ5	240	128	64	144	120	120	60	16	16	3.16	268
	TJ6	240	128	60	140	120	120	60	20	20	3.16	268
8	Fitted & fir	170	140	100	175	70	100	48	-	-	3.7	830
	Loose &fir	170	140	100	175	70	100	47	-	-	3.7	830
	Fitted & pine	170	140	100	175	70	100	48	-	-	5	1158
	Loose & pine	170	140	100	175	70	100	47	-	-	5	1158
9	LJ-1	390	210	160	315	195	195	95	0	5	4.18	1024

Note. Ref. 1-9 corresponds respectively to papers by Chen and Qiu (2016), Xu et al. (2018), Chen et al. (2017), Zhao et al. (2010), Gao et al. (2015), Chun et al. (2016), Xue et al. (2020), Su et al. (2020) and He (2019).